Journal of Structural Geology 86 (2016) 200–210

Contents lists available at ScienceDirect

Journal of Structural Geology

journal homepage: www.elsevier.com/locate/jsg

High precision analysis of an embryonic extensional fault-related fold using 3D orthorectified virtual outcrops: The viewpoint importance in structural geology

Stefano Tavani [a,*], Amerigo Corradetti [a], Andrea Billi [b]

[a] DiSTAR, Università Federico II, Napoli, Italy
[b] Consiglio Nazionale delle Ricerche, IGAG, Rome, Italy

A R T I C L E I N F O

Article history:
Received 17 December 2015
Received in revised form
11 March 2016
Accepted 16 March 2016
Available online 23 March 2016

Keywords:
Extensional fault-propagation
Virtual outcrop
Photogrammetry
Data analysis

A B S T R A C T

Image-based 3D modeling has recently opened the way to the use of virtual outcrop models in geology. An intriguing application of this method involves the production of orthorectified images of outcrops using almost any user-defined point of view, so that photorealistic cross-sections suitable for numerous geological purposes and measurements can be easily generated. These purposes include the accurate quantitative analysis of fault-fold relationships starting from imperfectly oriented and partly inaccessible real outcrops. We applied the method of image-based 3D modeling and orthorectification to a case study from the northern Apennines, Italy, where an incipient extensional fault affecting well-layered limestones is exposed on a 10-m-high barely accessible cliff. Through a few simple steps, we constructed a high-quality image-based 3D model of the outcrop. In the model, we made a series of measurements including fault and bedding attitudes, which allowed us to derive the bedding-fault intersection direction. We then used this direction as viewpoint to obtain a distortion-free photorealistic cross-section, on which we measured bed dips and thicknesses as well as fault stratigraphic separations. These measurements allowed us to identify a slight difference (i.e. only 0.5°) between the hangingwall and footwall cutoff angles. We show that the hangingwall strain required to compensate the upward-decreasing displacement of the fault was accommodated by this 0.5° rotation (i.e. folding) and coeval 0.8% thickening of strata in the hangingwall relatively to footwall strata. This evidence is consistent with trishear fault-propagation folding. Our results emphasize the viewpoint importance in structural geology and therefore the potential of using orthorectified virtual outcrops.

1. Introduction

Among several applications that digital representations of outcrops hold for structural geology and geosciences, perhaps one of the most important is the possibility of looking at the photo-realistic virtual outcrop, of almost any dimension, in orthographic projection mode. This capability would allow geologists to virtually orthorectify the outcrop with respect to any direction of interest (Fig. 1; e.g. fold axis, fault slip-normal direction, fracture-bedding intersection) to obtain, directly on the computer monitor, true measurements of geological features such as bed thickness and fault displacement for optimally oriented and undistorted photo-realistic cross-sections. Such an innovation is particularly important to geologists dealing with outcrop-scale geometries.

In natural outcrops, measurements of geological features such as fold interlimb angle, fault displacement, unconformity angle, bed thickness, and many others, can be affected by errors of various origins. They can be particularly large where a strong obliquity between the exposure and the proper direction of measurement exists, and where it is necessary to project structures from different portions of outcrops with complex 3D geometries. In particular, this measurement problem may affect outcrop-scale geological structures for which direct observations and measurements along proper directions may be impractical. For example, the measurements accuracy of fault stratigraphic separation or thickness of individual beds of stratigraphic sections for 10 to 100-m-sized structures can be greatly affected by the orientation of the structure

* Corresponding author.
E-mail addresses: stefano.tavani@unina.it (S. Tavani), amergeo@gmail.com (A. Corradetti), andrea.billi@cnr.it (A. Billi).

http://dx.doi.org/10.1016/j.jsg.2016.03.009
0191-8141/

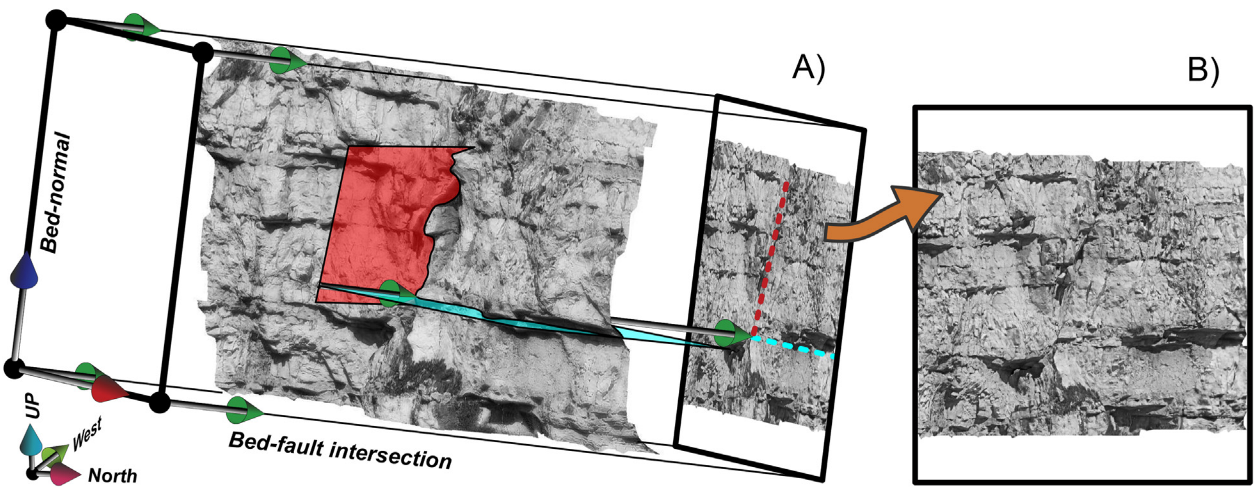

Fig. 1. Orthorectification of a Virtual Outcrop Model (VOM) along a direction of interest. This procedure essentially consists of two steps. (A) Geological features are digitized in the model, to compute the viewing direction of interest, which in this image the intersection between bedding (blue) and the fault (red). (B) Desired viewpoint shown as orthographic projection. (For interpretation of the references to color in this figure legend, the reader is referred to the web version of this article.)

with respect to the exposure and/or issues of accessibility limitations. Yet, improving these types of measurements is important, and sometimes essential, for effectively characterizing and interpreting many geological systems for attributes, such as with the geometry, kinematic history and operative deformation mechanisms for accommodation of displacement changes by the hangingwall rocks of dip-slip faults, particularly embryonic ones, which are commonly conducted at natural outcrops (e.g. Ferrill et al., 2012). The alternative of using seismic-reflection data that are three-dimensional and digital, so that photo-realistic profiles would not be needed, is not a viable option for these types of analyses because the technique lacks the resolution and accuracy for yielding the needed information to successfully characterize and interpret these structural systems (e.g. Torvela and Bond, 2011). Consequently, resolution at the finer scale using undistorted photo-realistic cross sections is needed to ascertain attributes, such as the subtleties of thickness variations of layers within one or more structures.

These types of data are essential for distinguishing kinematic behaviors such as the occurrence of trishear (Erslev, 1991; Hardy and McClay, 1999; Zehnder and Allmendinger, 2000) vs. flexural-slip (Donath and Parker, 1964; Tanner, 1989) for fault-related folds (Fig. 2). In particular, the mechanism of trishear fault propagation (e.g., Erslev, 1991; Hardy and Ford, 1997; Allmendinger, 1998; Zehnder and Allmendinger, 2000), requires that: (1) the rock has no major anisotropies; and (2) a triangular zone (named trishear) of strain-compatible and layering-insensitive shear is pinned to the fault tip (Fig. 2a). During fault propagation and displacement, while the hangingwall and footwall rock volumes are rigidly translated, the layers in the trishear zone preserve their cross-sectional area by modifying dip, length and thickness, and progressively developing a folded panel dipping in the same sense as the fault (named a synthetic monocline). The strain magnitude within the trishear zone as well as the thickness variation, and the dip and width of the synthetic monocline, is influenced by parameters such as the fault *propagation to slip ratio* (e.g. Allmendinger, 1998). The greater this ratio, the less strain within the trishear zone, the dip of the monocline, and the thickness variation between the hangingwall and the footwall. Conversely, extensional fault-propagation folding developed by constant bed-thickness flexural-slip folding, assumes that layering is a major anisotropy that is sheared during folding. This kind of extensional folding behavior also forms a synthetic monocline (Fig. 2b), which grows by kink-band migration, where the active axial surface is pinned to the fault tip (Tavani et al., 2006). Thickness of layers is preserved by definition but the area is not, due to layer-parallel stretching (Tavani et al., 2006). As normal displacement and coeval upward propagation of the fault continues, the width of the synthetic monocline increases, while its dip remains constant. Similarly to trishear fault-propagation, the dip of the monocline depends on the slip to propagation ratio. However, in this case, the relationship between the propagation to slip ratio (P/S) and the hangingwall cutoff angle is univocally defined for a given fault dip (Tavani et al., 2006).

Although these kinematic behaviors differ, the geometries for trishear and flexural-slip fault-propagation folds can converge for large propagation to slip ratios (Fig. 2c). Nonetheless, differences between thickness of strata in the hangingwall and in the footwall remain a diagnostic feature of trishear fault propagation, provided that it is possible to demonstrate that they are sufficiently sensitive to support the interpretation, rather than lying within overlapping values for the two scenarios. Accordingly, recognizing trishear fault-propagation folds with a large fault propagation to slip ratio can be a difficult task at the outcrop scale because uncertainties about bed thickness measurements along the outcrop with complex 3D surfaces may prevent structural geologists from distinguishing between trishear and flexural-slip. The use of digital representations of outcrops can allow structural geologists to overcome this data issue by providing the possibility of performing accurate and precise measurements of bed thicknesses and fault displacements.

In this paper, we present an example of a straightforward technique for producing orthorectified sections of virtual outcrops. Our main aim is to illustrate the workflow and the utility of this technique for fault and fold analysis at the outcrop scale. We will show that the use of high-resolution 3D orthorectified virtual outcrops allows identification of very small differences (about 0.5°) between the hangingwall and footwall cutoff angles and hangingwall layer thicknesses (0.8%). Thus, we are able discard flexural-slip folding for trishear fault-propagation folding. Our results emphasize the importance of viewpoint in geology and therefore, the potential of orthorectified virtual outcrops for achieving preferred viewpoints.

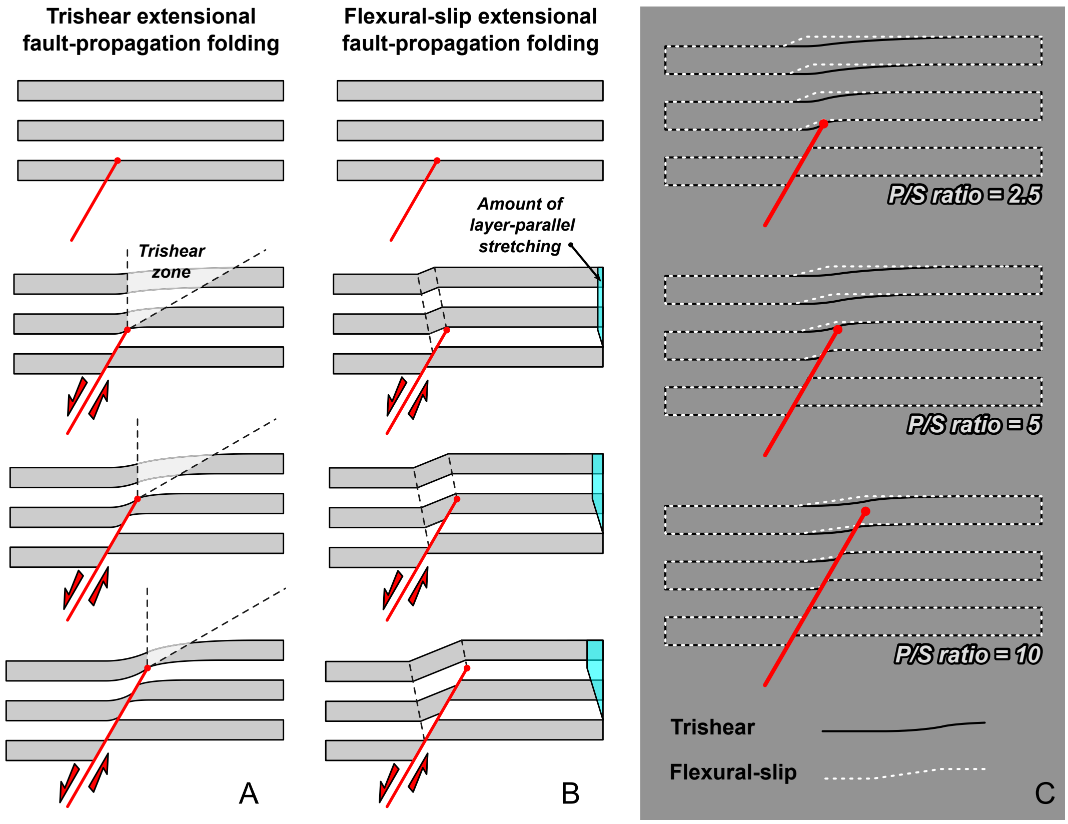

Fig. 2. Schematic illustration for the evolution of extensional fault-propagation folds developing by (A) trishear and (B) constant-thickness flexural-slip, respectively. (C) Sheme showing the overly of the two solutions for different values of the fault propagation to slip ratio. The trishear solution was drawn by using the FaultFold software by R. Allmendinger.

2. General method and error estimate

Remote sensing techniques for the acquisition of 3D terrain information have evolved rapidly in the last twenty years, leading to the ability to produce detailed 3D virtual outcrop models (VOM) for several different applications (e.g. Xu et al., 2000; Pringle et al., 2001; Bellian et al., 2005; Clegg et al., 2005; Trinks et al., 2006; McCaffrey et al., 2008; Abellán et al., 2014). Light detection and ranging technique (LiDAR) provides high-resolution point-clouds of complex target surfaces, and is currently the most popular technique for producing accurate virtual outcrop models (Hodgetts, 2013). However, logistic and cost limitations due to LiDAR equipment being expensive, bulky, and heavy, presently prevent its widespread use in the geological community. An alternative low-cost and versatile technique for producing VOMs is stereo-photogrammetry, which also ensures fast and uncomplicated draping of photographs onto the virtual model (Remondino and El-Hakim, 2006). This technique reconstructs a 3D scene from correlation of points in partly overlapping photographs taken from different positions, which is analogous to human vision that integrates information from two eyes. Recent advances both in computational speed and resolution of digital-imaging devices position the photogrammetric technique to easily and rapidly produce VOMs from photographs taken with conventional digital cameras (Pringle et al., 2001; Lebel et al., 2001; James and Robson, 2012; Favalli et al., 2012; Tavani et al., 2014; Reitman et al., 2015; Bistacchi et al., 2015).

Given a set of partly overlapping photographs pointing at the same scene, structure from motion algorithms (SFM; Ullman, 1979) can detect common suites of points or point clusters in the different photographs. The knowledge of these common points and their coordinates in the different photographs enables computation of the parameters that relate the X, Y, and Z coordinates of a point in a combined common space for the population of photographs to its X_n and Y_n position in the nth photograph as a function of camera position, orientation, and focal length. This procedure ensures the representation of an object surface seen in overlapping photographs as a point-cloud (Szeliski, 2010). Modern SFM algorithms are implemented in many software products facilitating the easy creation of 3D models for target objects, including geological outcrops. Many software products also support the transformation of point clouds into suites of meshes composed of irregular triangles that can be automatically draped with images producing 3D photorealistic textured meshes. Among the available software products, we used Agisoft Photoscan (e.g. Verhoeven, 2011) (www.agisoft.ru).

Recent studies have certified that the accuracy of the image-based models from photogrammetric assembly of a set of overlapping photographs equals or are comparable to the accuracy of models produced by LIDAR-based construction (e.g. Adams and Chandler, 2002; Harwin and Lucieer, 2012). However, a major issue for image-based VOM is that errors and distortions cannot be assessed a priori. The evaluation of the 3D distribution of the X, Y, and Z components of the error in the image-based model requires the knowledge of the position of a large number of points. Creating the spatial information for a large number of points in the model can require the use of LiDAR or totalstation equipment, which would potentially defeat the point of using photogrammetric imagery. Fortunately, a slightly less accurate estimate of the error and distortion can be obtained with cheap and portable tools: a compact laser distance meter, a compass, a laser level mounted on a tripod with a graduated dial, and some coded targets to be positioned on an outcrop (Fig. 3a). In the field (Fig. 3b), using the compass, the graduated dial on the tripod is oriented with respect to North, and represents the origin of our local reference system. The laser level is used to record the positions of a suite of coded targets (here called “coordinate targets”) at altitude zero, which is defined as the same elevation of the level, with the graduated dial and the laser distance meter providing the angular coordinate (azimuth angle) and the distance from the origin (i.e. the laser level), respectively.

For our study, we used these tools and this procedure to assess model errors and distortions. In particular, for the coded targets, we provided the spherical coordinates with the precision of 1° for the azimuth, 0.29° for the zenith, and 1.5 mm for the radius (errors provided by the equipments manufacturers). We placed additional targets (hereafter named “random targets”) at arbitrary positions on the outcrop and measured their distance from the origin of the local reference system using the laser distance meter (Fig. 3b) As targets (both coordinate and random ones) are used to evaluate the occurrence of distortions in the model, they require a good distribution around the outcrop surface. In fact, where accessibility limitations prevent the positioning of coded targets, they were replaced by points lit with a green laser pointer, as explained below. It is worth remarking that coordinate and random targets are identical (coordinate targets appear in red in Fig. 3b to facilitate their recognition in the figure). The only difference between them is that for the coordinate targets, we measured the three polar coordinates, while for the random ones we measured only the radius but neither the azimuth nor the zenith angles. For the 3D digital model, we used the position of the coordinate targets to re-scale and re-orient the model itself. We then computed the position of all targets in the scaled 3D digital model and compared the distances between the targets and the origin (i.e. the radius of the spherical coordinates) as measured in the real world and in the digital environment. We used the average value of this difference as a proxy of the model error. We then plotted this difference vs. the X, Y, and Z coordinates of each target to demonstrate that the error is not dependent on these components and thus that the model is not affected by significant distortions.

3. Case study

The study outcrop consists of a barely accessible steep cliff located close to the town of San Severino Marche (the origin of the model is Lat: 43°13′28,70″N; Long:13°07′01.81″E), along the external (eastern) front of the northern Apennines fold-thrust belt, Italy. In particular, the outcrop is located in the crest of the Sibillini anticline (Fig. 4). This fold is a N–S-striking and E-verging thrust-related anticline that constitutes the mountain front of the Northern Apennines, and deformed the exposed Mesozoic and Cenozoic limestones and marls, and the overlying thick (up to many km) siliciclastic sequence (Pierantoni et al., 2013). The anticline is affected by a pervasive extensional deformation pattern, which includes sub-seismic joints and normal faults striking mostly parallel but also perpendicular to the anticlinal trend. Only one of the normal faults reaches a length exceeding a few tens of meters, so that it is observable at map-scale, and it is exposed in the southern portion of the map (Fig. 4). The N–S striking extensional structures are principally located in the anticlinal crest and represent late-folding structures, which are interpreted as forming in response to the rapid and abrupt uplift of this mountain front anticline (Tavani et al., 2012).

The study outcrop exposes shallow-dipping Mesozoic carbonates of the Maiolica Formation, consisting of about 20-cm thick, well bedded micritic limestone with silica beds and thin clay interlayers, affected by a few embryonic extensional faults belonging to the late-folding set (Fig. 5a). We positioned the laser level at about 10 m from the outcrop and following our procedure, we used the level with the laser pointer to place three coordinate targets on the outcrop (Fig. 5b), where all these targets were at the same elevation as the laser level that is the origin of our reference system. The maximum expected vertical error on the positioning for these targets is about 5 cm, because the error on the horizontal determination of the level is ±0.29° and the average distance between the targets and the origin of the reference system is about 10 m. Two additional random targets were positioned in the lower part of the outcrop. Moreover, as we could not position coded targets in

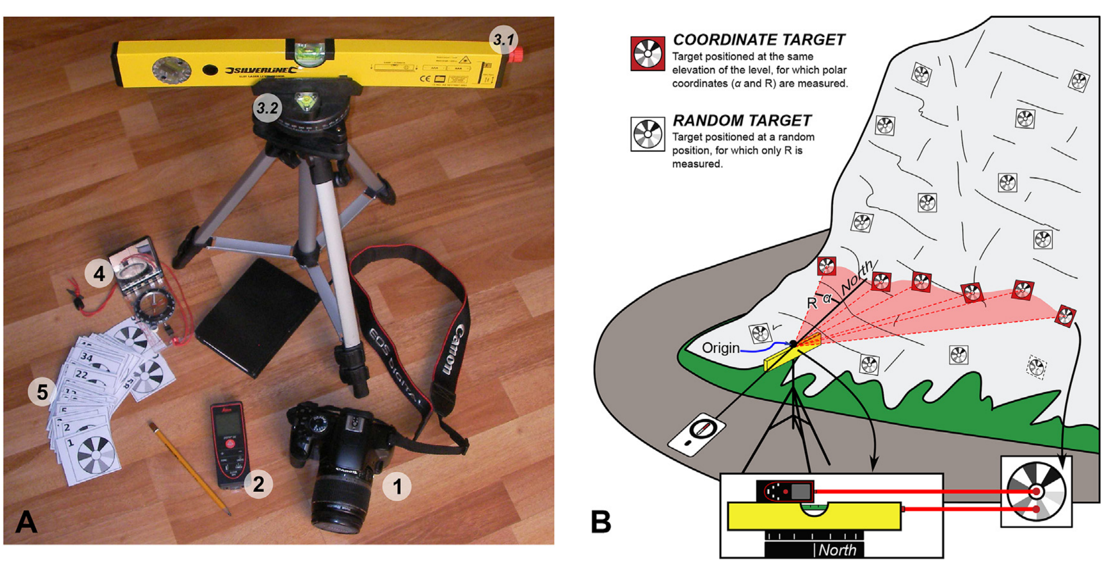

Fig. 3. (A) Field devices used in this work: (1) Canon EOS 450D camera. Photograph resolution is set to 4272 × 2848 pixel. (2) Leica DISTO D2 laser distance meter (0.05–60 m measuring range, accuracy = ± 1.5 mm). (3) Silverline equipment including (3.1) a 40 cm long level (error on the horizontal determination is ±0.29°) with a laser pointer and (3.2) a tripod with a graduated rotating base (accuracy = 1°). (4) Silva compass. (5) Coded targets. (B) Scheme showing the field use of compass, laser distance meter, laser level, and rotating base to place a first suite of targets in the outcrop and to get their polar coordinates (coordinate targets: red targets in the figure). Additional targets (random targets: white targets in the figure) are arbitrarily placed and only their distance from the origin is measured. (For interpretation of the references to color in this figure legend, the reader is referred to the web version of this article.)

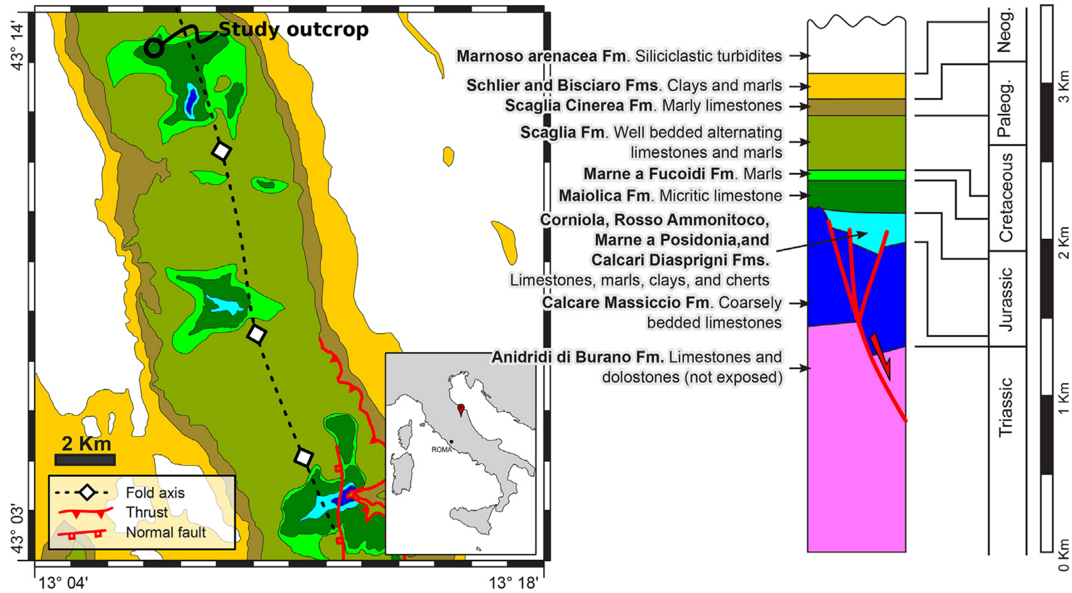

Fig. 4. Geological map and stratigraphic sequence for the Sibillini anticline in the northern Apennines. The location of the study outcrop is shown in the map.

the upper portion of the cliff, we used an additional laser pointer with a long-distance highly visible green light to position eight other random points, that were contextually photographed (Fig. 5c). We used a Canon EOS 450D camera to take 156 photographs (4272 × 2848 pixel resolution) of the outcrop.

Only the lower part of the outcrop is accessible and the cliff can be photographed only from ground level. Accordingly, to cover the upper part of the outcrop with at least two sets of photographs, we took photographs at different distances from the outcrop (5–15 m) and with different focal lengths, which resulted in an approximate photograph's resolution ranging from 1 to 0.2 pixel/mm^2. As detailed below, despite the different acquisition strategies, errors for point positions in the upper and lower portions of the outcrop have almost the same negligible value.

Photographs were imported into the Agisoft Photoscan software, where we selected a sub-area of the outcrop with a surface of approximately 250 m^2. A point-cloud of 3.5 × 10^6 points with a resolution of about 1.4 points/cm^2 was generated (Fig. 5d). The subsequent 3D triangulation of points allowed us to obtain a triangular mesh made of 5 × 10^6 irregular triangles that had an average area of about 0.5 cm^2 each. After identifying all targets in the model (Fig. 5d), we used the coordinate targets alone to re-scale and re-orient the model. Finally, we used all targets in the scaled model to estimate the model's error, which is the difference between the distance of target from the origin measured in the field and in the corresponding digital environment. This difference ranges between about −4 and 6 cm (Fig. 6a). Only one target was affected by a large location error (i.e. 20 cm; this target is identified with a red circle in Fig. 5d), and so we discarded it from the model due to possible measurement error. By removing this anomalous value, we obtained an average value for the absolute error of 2.8 cm. As previously explained, we also plotted the error versus the X, Y, and Z coordinates of the corresponding target (Fig. 6b). This diagram shows that the error neither increases nor decreases with the X, Y, and Z coordinates. In essence, Fig. 6b demonstrates that the error is insensitive to the position of the target, thus indicating that the error is random, and not a function of position or direction.

Subsequently, we imported the textured mesh into the OpenPlot software (Tavani et al., 2011, 2014), where we obtained the orientation of geological surfaces directly from their digital geometry in the model (Hodgetts et al., 2004; Trinks et al., 2006). This procedure involved point picking along the intersection between the particular geological surface and the outcrop's surface. The same procedure involved also the subsequent extraction of the maximum component of the moment of inertia of these points (i.e. the vector orthogonal to the best-fit plane; Fernández, 2005, Fig. 7a and b), provided that picked points are highly coplanar and poorly colinear. Using this procedure, we digitally measured a total of 248 meso-structures: 58 bedding surfaces, 140 joints, and 50 segments of the studied fault (Fig. 7c) (raw attitude data, including values of azimuth, dip, and data type, are available as text file in the Supplementary material). In the plot (Fig. 7c), bedding surfaces identify a single maximum corresponding to a N302°-striking and NE3°-dipping plane, with a very slight difference between the footwall (strike is 321° and dip is 4°) and the hangingwall (strike is 294° and dip is 3°). Joints have two orientation maxima consisting of high-angle-to-bedding surfaces striking ESE-WNW and NNE-SSW, respectively. The digitalized segments of the extensional fault are clustered around a single maximum corresponding to a N191°-striking and NW74°-dipping plane. From these data, we derived two mutually orthogonal directions: the bedding-fault intersection direction and the bedding-normal direction based on average bedding value. We used these directions together with the one orthogonal to both to reorient the VOM in Photoscan so as to obtain, in orthographic projection view, an undistorted frontal view of the plane perpendicularly to bedding and the fault (Fig. 1). We exported a 4-pixels/cm orthorectified view of the outcrop obtained from this observation point (Fig. 8). Successively, we imported this orthorectified image in the Inkscape open-source software for vector graphic drawing (www.inkscape.org), where we traced beds and fault segments (Fig. 9a), as it is usually done when picking horizons in a seismic profile. On this line drawing (Fig. 9a), we digitally measured true dips and stratigraphic displacements. In addition, we correlated cutoff points of the hangingwall and footwall strata and constructed a stratigraphic separation diagram (Fig. 9b).

The fault includes two strands (named *i* and *ii* in Fig 9b) separated by an area where layers are folded and unfaulted (Fig. 9a and b). The fold is particularly evident for a chert layer between the two non-coplanar strands of the fault (Fig. 9c). In this folded area, we

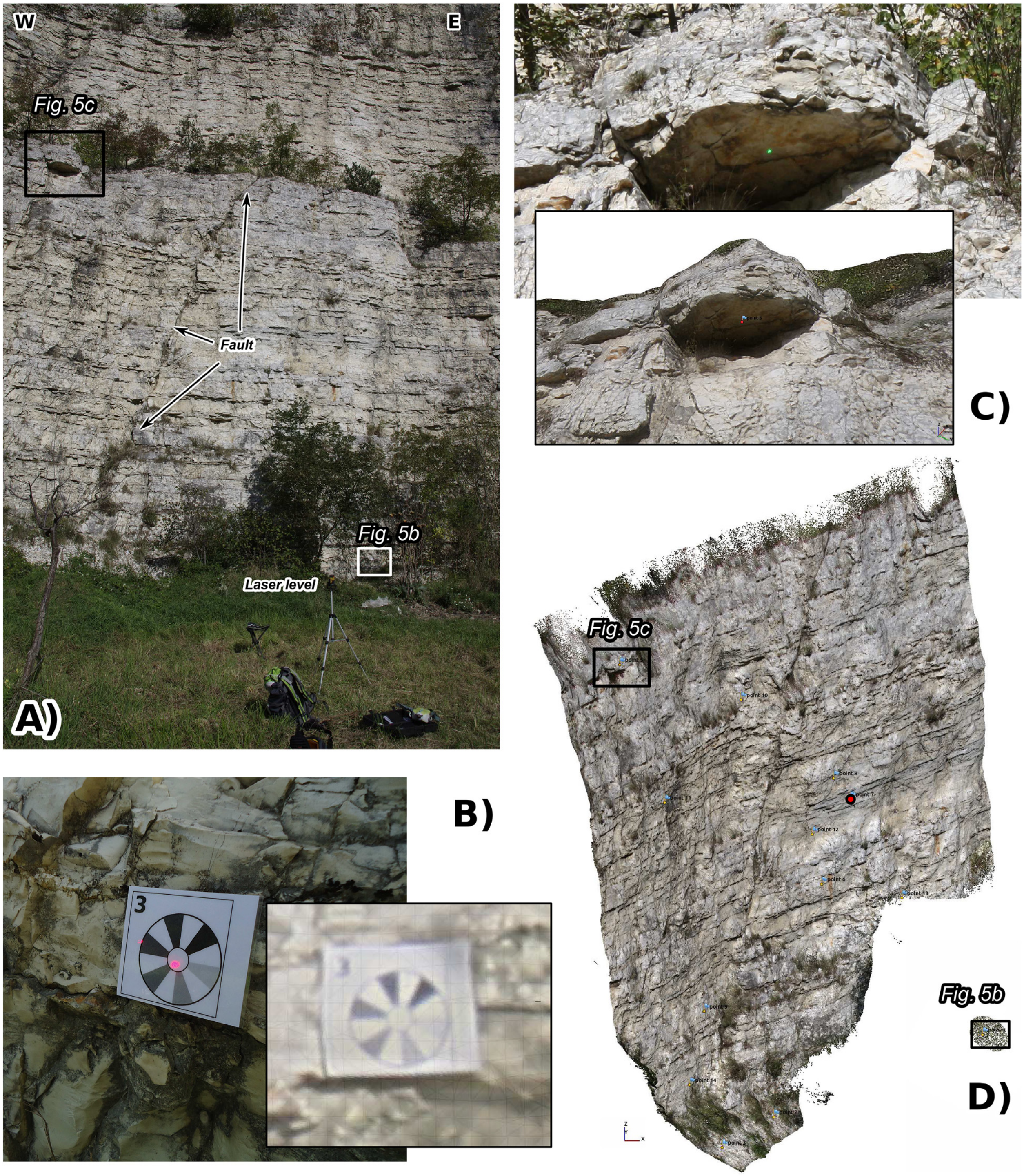

Fig. 5. (A) Photograph of the San Severino outcrop showing the near vertical cliff and the embryonic normal fault along with the laser level, plus the target point for (B) and (C). (B) Example of a target point made with a coded target, as seen in the real world and in the digital environment. The two red lights seen in the target correspond to the pointers of the level and distance meter, respectively. (C) Example of a target point made with a green laser light, as seen in the real world and in the digital environment. (D) RGB colored point cloud of the outcrop, with position of targets indicated by blue flags. The red circle indicates a target with a high positioning error (i.e. 20 cm). (For interpretation of the references to color in this figure legend, the reader is referred to the web version of this article.)

computed the stratigraphic separation that would have been predicted if a fault strand rather than a fold was present, based on projecting separation magnitudes from along the fault strands into the unfolded fault domains (Fig. 9b). We also measured the dip of digitized bedding traces in the hangingwall and footwall by computing the slope of the best-fit linear regression of the nodes of the digitized bedding traces (we used the function “slope” of the LibreOffice Calc software). In agreement with the slight difference between the strikes of bedding in the two walls of the fault, layers in the footwall and in the hangingwall have apparent dips of 0.8° and 0.3°, respectively (Fig. 9d). The 0.5° difference between hangingwall and footwall dips is almost constant along the entire pair of

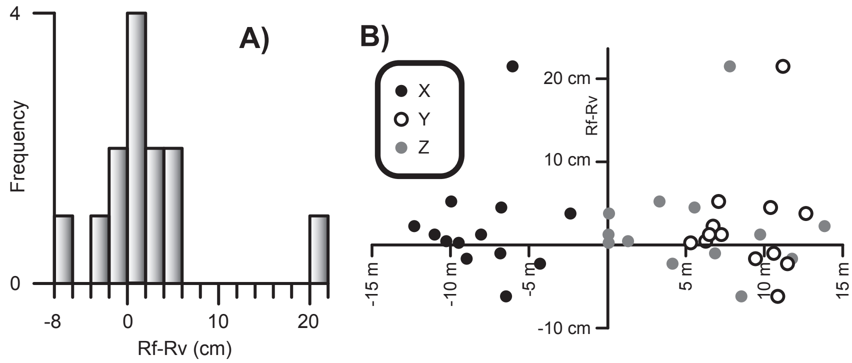

Fig. 6. Difference between measured (Rf) and digitally computed (Rv) distances of targets from the origin in the San Severino outcrop. (A) Frequency distribution of Rf-Rv. (B) Scatterplot with Rf-Rv values along the Y-axis and X, Y, and Z coordinates of the target along the X-axis of the plot.

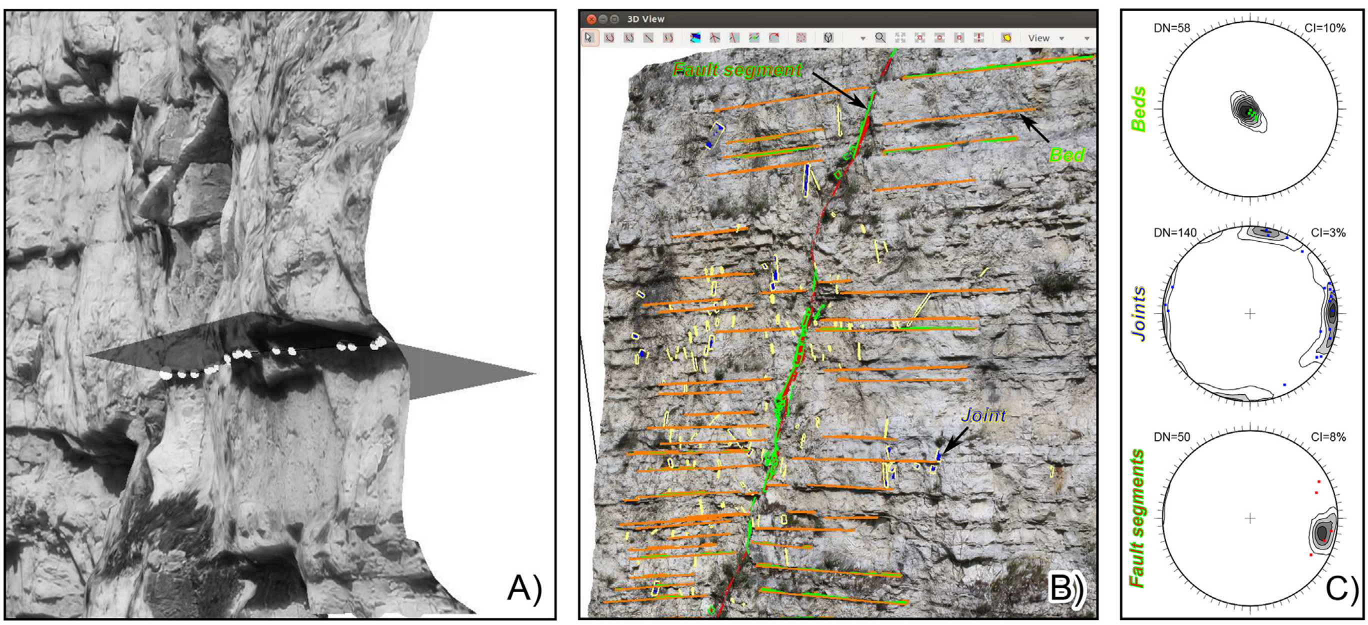

Fig. 7. (A) Close-up view of the model in OpenPlot, with example of a digitalized bedding trace (white points) and derived best-fit plane (medium gray planar polygon). (B) View of the San Severino VOM in OpenPlot, with digitized bedding surfaces (green polygons with orange border), fault segments (red polygons with green border), and joints (blue polygons with yellow border). (C) Frequency contour in stereographic equal-area projection of poles to digitalized bedding surfaces (green with orange border), joints (blue with yellow border), and fault (red with green border) segments. DN and CI refer to data number and contouring interval, respectively. In the stereoplots, the colored squares correspond to structures measured in the field with a clino-compass. (For interpretation of the references to color in this figure legend, the reader is referred to the web version of this article.)

fault strands.

4. Trishear vs. flexural-slip extensional fault propagation

Since trishear fault-propagation folding is based on forward modeling (Allmendinger, 1998), equations relating fault and fold shapes do not exist. Accordingly, to access the consistency of an observed fold with respect to the two possible kinematic behaviors, equations of flexural-slip fault-propagation folding are derived, illustrated and used for this analysis.

Let us consider a fault with a negligible displacement (Fig. 10a) with its tip lying in the layer L_0. After a certain amount of displacement, the tip of the fault has propagated upward, reaching layer L_1, and a synthetic monocline with a constant dip has developed, according to the constant bed-thickness flexural-slip construction illustrated in Fig. 2b. Equations (1) and (2) of Fig. 10a relate the fault slip, the fault propagation, and the distance between the initial and the final position of the tip measured in the hangingwall (DistanceH), to the footwall cutoff angle (α), the hangingwall cutoff angle (β), and the L_0-L_1 thickness (H). Combining Equations (1) and (2), allows the derivation of Equations (3) and (4), which relate the hangingwall and footwall cutoff angles to the fault slip (displacement), the propagation of the fault tip, and the fault displacement to distance ratio. To evaluate how much a natural extensional fold diverges from this model, we introduce a strata thinning/thickening coefficient (Fig. 10b). Thickness variations between hangingwall and footwall in faulted strata are allowed in this second model, using K the thinning/thickening coefficient. As a consequence of allowing variations in the thickness of strata, the amount of propagation of the fault is no longer measurable. Having introduced K, Equations (1) and (2) of Fig. 10a transform into Equations (5) And (6) of Fig. 10b, respectively. Since the propagation has been removed from the system of equations, we can relate cutoff angles only to the displacement to distance ratio (Equation (7)) and to the K coefficient (Equation (8)). These equations will be used to determine the applicability of the two

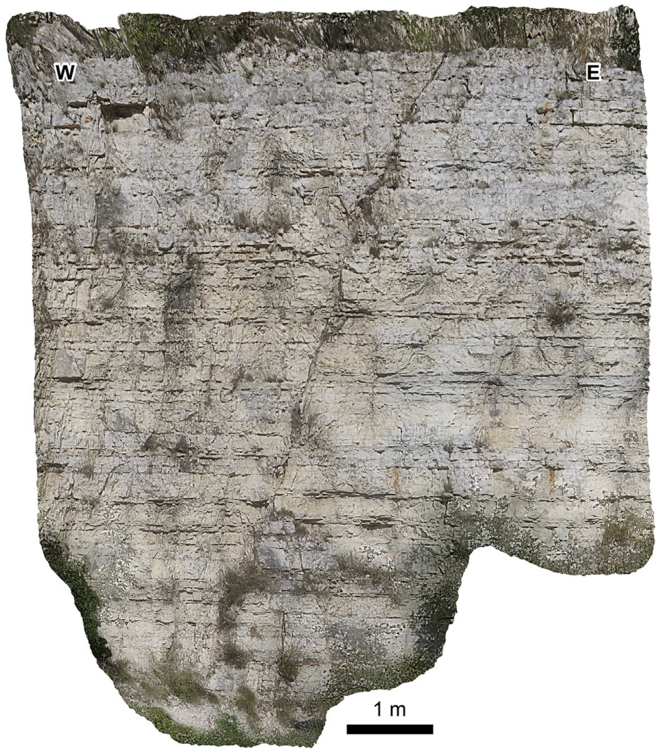

Fig. 8. Orthorectified photo for the study outcrop.

kinematic behaviors to accommodate propagation and displacement for this fault.

5. Discussion

5.1. Geometry of the fault and related fold

The fault studied in this paper cuts through the fractured limestone exposed near San Severino Marche in the Apennines. Our remotely sensed data (fault and joint attitude) show substantial strike-parallelism between the fault and one set of joints (Fig. 7b). Locally, the fault also has cutoff angles of about 90° (Fig. 9c). Therefore, we infer that fault growth included progressive linkage of pre-existing bedding-perpendicular joints with displacement variation on these incorporated joints as a function of the timing of linkage versus the displacement history. This postulated fault-propagation history has been observed in many faults with small displacements that offset sedimentary layers with bed-normal joints (Graham et al., 2003; Crider and Peacock, 2004; Healy et al., 2006; Petracchini et al., 2012, 2015) and often manifests a steep fault attitude (e.g., average dip is > 70°) that would be mechanically unfavorable in a typical (Andersonian) dynamic setting with no pre-existing weaknesses (e.g. joints) in the rocks.

The precise measurements of stratigraphic separations in the inaccessible portion of the fault were made possible by image-based modeling and orthorectification. These measurements have an accuracy of 1 cm, which is the resolution of the Virtual Outcrop Model, along the 7-m-long composite fault trace. Although we did not identify kinematic indicators along the fault, structural studies in this area indicate that N–S-striking faults are characterized by a normal dip-slip kinematics (e.g. Tavani et al., 2012). The inference of a dip-slip kinematics for our study fault in nearly sub-horizontal strata, allows us to assume that the stratigraphic separation diagram in Fig. 9b exactly corresponds to a displacement–distance diagram (e.g. Muraoka and Kamata, 1983; Williams and Chapman, 1983). Using this assumption, fault displacement shows a quasi–-linear relationship with position along the fault (Fig. 9b), as previously documented for small-scale low-displacement normal faults (Dawers et al., 1993). Also, as the displacement decrease upward along the fault trace, we infer that the fault propagated upward (Ellis and Dunlap, 1988; Hughes and Shaw, 2014).

5.2. Testing trishear vs flexural-slip solutions

Upward propagating faults in extensional setting commonly lead to the development of synthetically dipping monoclines (i.e. panels dipping in the same sense as the underlying fault; Freund, 1979; Withjack et al., 1990; Schlische, 1995; Gawthorpe et al., 1997; Ferrill et al., 2004; Tavani et al., 2015). In particular, the synthetic monocline accommodates hangingwall downthrow in the unfaulted strata ahead of the fault tip, and its geometry is linked to the ratio between propagation and slip of the fault, as illustrated in Figs. 2 and 10. In section 4, we derived equations linking cutoff angles of hangingwall and footwall, and the displacement–-distance ratio for flexural-slip extensional fault-propagation folds (Equations (3) and (4) of Fig. 10a). We have also introduced a thickness variation coefficient between hangingwall and footwall strata (i.e. the K coefficient of Fig. 10b), to test the deviation of natural folds from the bed thickness preservation, and so to evaluate if the fold approaches a trishear solution.

In the study outcrop, as previously discussed, we derived a footwall cutoff angle (α angle of Fig. 10) of 70°, an hangingwall cutoff angle of 70°–0.5° (i.e. the β angle of Fig. 10 is 69.5°). Displacement–distance ratio is provided by the slope of the linear regression in the graph of Fig. 9b, and it is 0.0121. Using these values in Equation (8) of Fig. 10b, results in a K coefficient of 1.00876, which means that either the hangingwall has thickened 0.88% or the footwall has thinned 0.87%, or a combination of both. Notice that such a thickening cannot be attributed to the occurrence of an hangingwall dip component perpendicular to the section, because this component is less than 1° and has a negligible effect on the measured thickness (K would be about 1.0001).

To visually test the accuracy of the result, we removed the differential rotation between hangingwall and footwall, using values provided in Fig. 9d, and we restored the hangingwall to its original thickness, assuming no thinning of the footwall. The result is illustrated in Fig. 11, where gray layers in the background facilitate the comparison of dip and thickness between strata in the footwall and in the hangingwall. The graph shows an impressive match, supporting the accuracy of the reconstruction and the lack of internal bends in the hangingwall strata.

A check of this result is done by computing the theoretical displacement–distance relationship, and hangingwall and footwall cutoff angles for the fault in the absence of strata thinning/thickening. This case corresponds to an extensional synthetic monocline entirely developed by flexural-slip folding, where only layer-parallel strain is allowed. Using measured hangingwall and footwall cutoff angles, and imposing a K coefficient of 1 yields a displacement–distance ratio of 0.0034, instead of the measured 0.0121. To attain such a ratio, the studied fault should have either about 8 cm less of displacement in its lower portion or 8 cm more in its upper portion, or a combination of both. These values exceed the resolution limitations for the VOM, which is about 1 cm, and they were not identified as existing in the VOM, supporting the idea that strata thickness were modified during folding. Similarly, using the measured displacement–distance ratio of 0,0121 as an input parameter, in combination with the footwall cutoff angle of 70° (i.e. the measured fault dip), returns the expected hangingwall cutoff

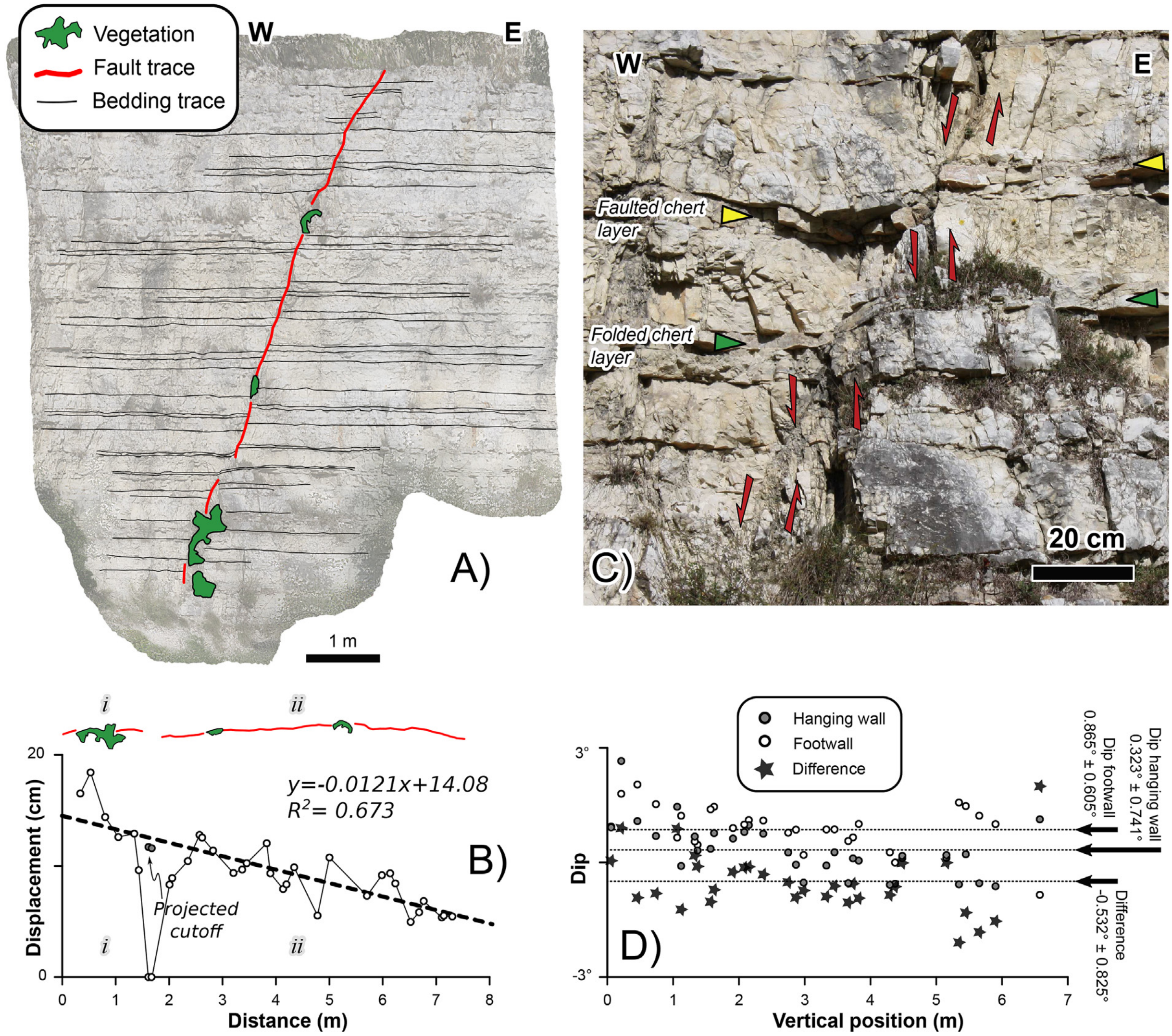

Fig. 9. (A) Line-drawing of layers and fault segments. (B) Fault stratigraphic separation diagram constructed using cutoff points (white circles) and non-folded cutoff points derived by projecting the layer outside the folded areas (black circles). (C) Detail of the overstep area between the two fault segments, illustrating the folded but unfaulted chert layer, and many bedding perpendicular strands of the fault. (D) Dip of layers in the hangingwall and footwall (and their difference) versus their stratigraphic elevation (0 is the bottom of the outcrop).

angle of 68.2°, instead of the measured 69.5°, which is a difference of about 1.3°. The difference is almost twice the standard deviation of the measured difference between hangingwall and footwall strata dip (Fig. 9d), so it is not validated by data from the VOM. Finally, using the measured displacement–distance ratio and the measured dip of strata, a K coefficient of 1 would imposes a fault dip of about 37°, which was definitely not observed.

In conclusion, to achieve the measured displacement–distance ratio, a tilting of layers and internal deformation by strata thickening (or thinning) is needed, contributing about 30% and 70%, respectively, to the displacement of the fault. Consequently, we infer that the hangingwall fold is not just the result of flexural-slip, but rather the occurrence of stratal thickening in the downthrowing hangingwall, consistent with the trishear extensional fault propagation folding (e.g. Erslev, 1991; Allmendinger, 1998; Hardy and McClay, 1999; Johnson and Johnson, 2001; Jin and Groshong, 2006; Jackson et al., 2006; Mitra and Miller, 2013). For this interpretation, the triangular shear zone pinned at the upward-propagating fault tip created the synthetically dipping monocline where strata thickness was not preserved.

6. Conclusions

We conclude that the growth model of a small-scale, low-displacement normal fault exposed in a nearly inaccessible site can be inferred in a few simple steps starting only from a set of field photographs taken with entry-level reflex cameras. The advantages of the proposed method are its ease of use, low-cost, minimal amount of equipment, and suitability also for inaccessible outcrops, whereas the weaknesses are only those ones connected with the limits of the photographic technique and equipment. Hence, the workflow constitutes an efficient and straightforward method for field studies aimed at quantitatively analyzing geological features at the outcrop scale. The proposed method can easily allow researchers to create the desired, representative virtual profiles using proper orthorectification and viewpoint rotation.

The methodology has been applied to study an embryonic normal fault affecting shallow dipping limestones in the Apennines fold and thrust belt. Accurate measurements of the stratigraphic separations diagram and strata dip were made possible by the adopted procedure of photograph orthorectification. Measured

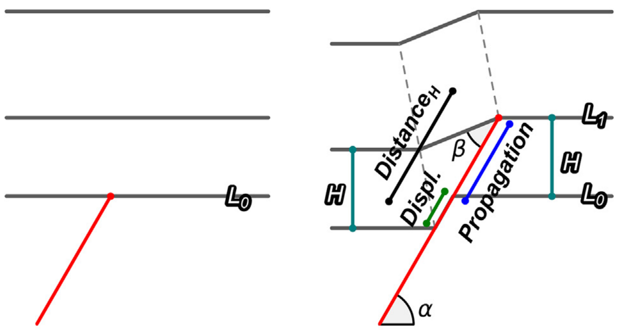

$$\text{(1)}\quad Propagation = Distance_H - Displacement = \frac{H}{\sin(\alpha)}$$

$$\text{(2)}\quad Propagation + Displacement = Distance_H = \frac{H}{\sin(\beta)}$$

$$\text{(3)}\quad \frac{Propagation}{Displacement} = \frac{\sin(\beta)}{\sin(\alpha)-\sin(\beta)}$$

$$\text{(4)}\quad \frac{Displacement}{Distance_H} = 1 - \frac{\sin(\beta)}{\sin(\alpha)}$$

A

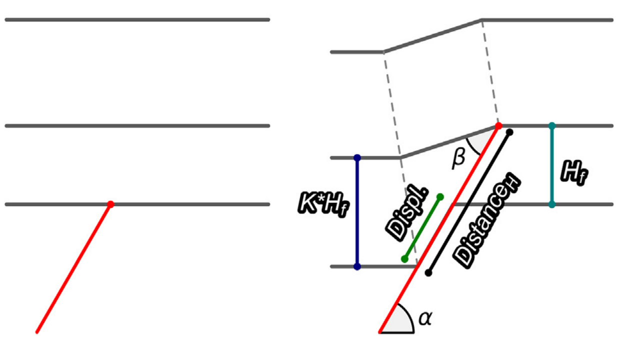

$$\text{(5)}\quad Distance_H - Displacement = \frac{H_f}{\sin(\alpha)}$$

$$\text{(6)}\quad Distance_H = \frac{K{*}H_f}{\sin(\beta)}$$

$$\text{(7)}\quad \frac{Displacement}{Distance_H} = 1 - \frac{\sin(\beta)}{K\sin(\alpha)}$$

$$\text{(8)}\quad K = \frac{\sin(\beta)}{\sin(\alpha)*\left(1-\frac{Displacement}{Distance_H}\right)}$$

B

Fig. 10. Schematic profiles showing a synthetic monocline developing in the hangingwall of an upward-propagating fault tip, with inset stating the relationships and equations for displacement as a function of position along the fault of a layer, to the footwall cutoff angle (α), and to the hangingwall cutoff angle (β). (A) Multilayer preserving the bed thickness during folding. (B) Multilayer for which thickness variations between footwall and hangingwall strata occur, with K the thickening coefficient.

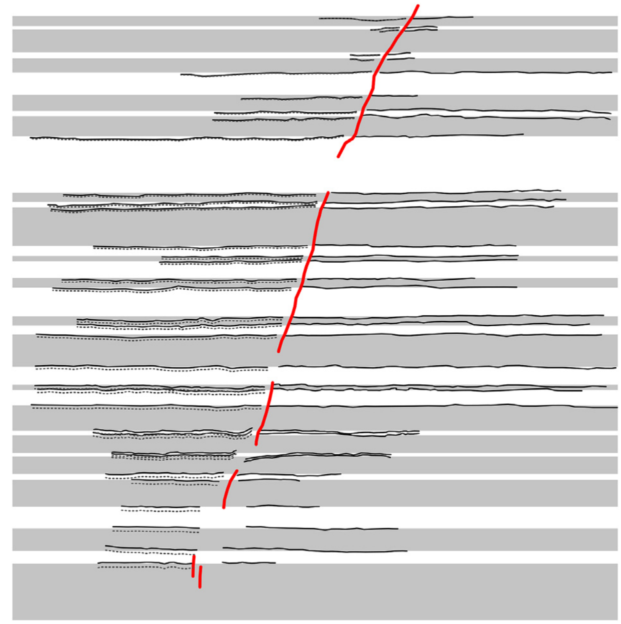

Fig. 11. Line-drawing of layers in Fig. 8(a) after removing the hangingwall and footwall layer dip across the fault (red traces). In the hangingwall, the black lines represent strata after thickening removal, whereas dashed dark gray lines represent strata with their present-day thickness. (For interpretation of the references to color in this figure legend, the reader is referred to the web version of this article.)

values of hangingwall and footwall dip, along with the displacement distance ratio, were compared with those expected for an idealized flexural-slip, extensional fault-propagation fold. Such comparison evidenced that folding was accompanied by 0.8% thickening of strata in the hangingwall relatively to footwall strata, which matches our observation. This strata thickening is consistent with trishear fault-propagation folding.

Acknowledgments

The authors are grateful to Steve Whitmeyer and Rick Groshong, and to the Editor William Dunne, for their valuable comments and suggestions which helped us to improve the manuscript.

Appendix A. Supplementary data

Supplementary data related to this article can be found at http://dx.doi.org/10.1016/j.jsg.2016.03.009.

References

Abellán, A., Oppikofer, T., Jaboyedoff, M., Rosser, N.J., Lim, M., Lato, M.J., 2014. Terrestrial laser scanning of rock slope instabilities. Earth Surf. Process. Landf. 39, 80–97.
Allmendinger, R.W., 1998. Inverse and forward numerical modeling of trishear fault-propagation folds. Tectonics 17, 640–656.
Adams, J., Chandler, J., 2002. Evaluation of lidar and medium scale photogrammetry for detecting soft-cliff coastal change. Photogramm. Rec. 17, 405–418.
Bellian, J.A., Kerans, C., Jennette, D.C., 2005. Digital outcrop models: applications of terrestrial scanning lidar technology in stratigraphic modeling. J. Sediment. Res. 75, 166–176.
Bistacchi, A., Balsamo, F., Storti, F., Mozafari, M., Swennen, R., Solum, J., Tueckmantel, C., Taberner, C., 2015. Photogrammetric digital outcrop reconstruction, visualization with textured surfaces, and three-dimensional structural analysis and modeling: innovative methodologies applied to fault-related dolomitization (Vajont Limestone, Southern Alps, Italy). Geosphere 11, 2031–2048.
Clegg, P., Trinks, I., McCaffrey, K., Holdsworth, B., Jones, R., Hobbs, R., Waggott, S., 2005. Towards the virtual outcrop. Geoscientist 15, 8–9.
Crider, J.G., Peacock, D.C.P., 2004. Initiation of brittle faults in the upper crust: a

review of field observations. J. Struct. Geol. 26, 691–707.
Dawers, N.H., Anders, M.H., Scholz, C.H., 1993. Growth of normal faults. Geology 21, 1107–1110.
Donath, F.A., Parker, R.B., 1964. Folds and folding. Geol. Soc. Am. Bull. 75, 45–62.
Ellis, M.A., Dunlap, W.J., 1988. Displacement variation along thrust faults: implications for the development of large faults. J. Struct. Geol. 10, 183–192.
Erslev, E.A., 1991. Trishear fault-propagation folding. Geology 19, 617–620.
Favalli, M., Fornaciai, A., Isola, I., Tarquini, S., Nannipieri, L., 2012. Multiview 3D reconstruction in geosciences. Comput. Geosci. 44, 168–176.
Fernández, O., 2005. Obtaining a best fitting plane through 3D georeferenced data. J. Struct. Geol. 27, 855–858.
Ferrill, D.A., Morris, A.P., Sims, D.W., Waiting, D.J., Hasegawa, S., 2004. Development of synthetic layer dip adjacent to normal faults. In: Sorkhabi, R., Tsuji, Y. (Eds.), Faults, Fluid Flow, and Petroleum Traps, American Association of Petroleum Geologists Memoir, vol. 85, pp. 125–213.
Ferrill, D.A., Morris, A.P., McGinnis, R.N., 2012. Extensional fault-propagation folding in mechanically layered rocks: the case against the frictional drag mechanism. Tectonophysics 576, 78–85.
Freund, R., 1979. Progressive strain in beds of monoclinal flexures. Geology 7, 269–271.
Gawthorpe, R.L., Sharp, I., Underhill, J.R., Gupta, S., 1997. Linked sequence, stratigraphic and structural evolution of propagating normal faults. Geology 25, 795–798.
Graham, B., Antonellini, M., Aydin, A., 2003. Formation and growth of normal faults in carbonates within a compressive environment. Geology 31, 11–14.
Hardy, S., Ford, M., 1997. Numerical modeling of trishear fault propagation folding. Tectonics 16, 841–854.
Hardy, S., McClay, K., 1999. Kinematic modeling of extensional fault-propagation folding. J. Struct. Geol. 21, 695–702.
Harwin, S., Lucieer, A., 2012. Assessing the accuracy of georeferenced point clouds produced via multi-view stereopsis from unmanned aerial vehicle (UAV) imagery. Remote Sens. 4, 1573–1599.
Healy, D., Jones, R.R., Holdsworth, R.E., 2006. Three-dimensional brittle shear fracturing by tensile crack interaction. Nature 439, 64–67.
Hodgetts, D., Drinkwater, N.J., Hodgson, D.M., Kavanagh, J., Flint, S., Keogh, K., Howell, J., 2004. Three-dimensional geological models from outcrop data using digital data collection techniques: an example from the Tanqua Karoo depocentre, South Africa. In: Curtis, A., Wood, R. (Eds.), Geological Prior Information, vol. 239. Geological Society of London, Special Publications, pp. 57–75.
Hodgetts, D., 2013. Laser scanning and digital outcrop geology in the petroleum industry: a review. Mar. Pet. Geol. 46, 335–354.
Hughes, A.N., Shaw, J.H., 2014. Fault displacement-distance relationships as indicators of contractional fault-related folding style. AAPG Bull. 98, 227–251.
Jackson, C.A.L., Gawthorpe, R.L., Sharp, I.R., 2006. Style and sequence of deformation during extensional fault-propagation folding: examples from the Hammam Faraun and El-Qaa fault blocks, Suez Rift, Egypt. J. Struct. Geol. 28, 519–535.
James, M.R., Robson, S., 2012. Straightforward reconstruction of 3D surfaces and topography with a camera: accuracy and geoscience application. J. Geophys. Res. 117. F03017.
Johnson, K.M., Johnson, A.M., 2001. Mechanical analysis of the geometry of forced-folds. J. Struct. Geol. 24, 401–410.
Jin, G., Groshong, R.H., 2006. Trishear kinematic modeling of extensional fault-propagation folding. J. Struct. Geol. 28, 170–183.
Lebel, D., Vuitton, R., Deblonde, C., Marcil, J.-S., Massé, L., Kirkwood, D., Vallée, M.A., De Roza, R., Malo, M., 2001. Integration of photogrammetric data in the construction of a 3-D geological model in a thrust-fold belt, Moose Mountain, Alberta, Canada. J. Virtual Explor. 4, 31–41.
McCaffrey, K.J.W., Feely, M., Hennessy, R., Thompson, J., 2008. Visualization of folding in marble outcrops, Connemara, western Ireland: an application of virtual outcrop technology. Geosphere 4, 588–599.
Mitra, S., Miller, J.F., 2013. Strain variation with progressive deformation in basement-involved trishear structures. J. Struct. Geol. 53, 70–79.
Muraoka, H., Kamata, H., 1983. Displacement distribution along minor fault traces. J. Struct. Geol. 5, 483–495.
Pierantoni, P., Deiana, G., Galdenzi, S., 2013. Stratigraphic and structural features of the Sibillini mountains (Umbria–Marche Apennines, Italy). Ital. J. Geosci. 132, 497–520.
Pringle, J.K., Clark, J.D., Westerman, A.R., Stanbrook, D.A., Gardiner, A.R., Morgan, B.E.F., 2001. Virtual outcrops: 3-D reservoir analogues. In: Ailleres, L., Rawling, T. (Eds.), Animations in Geology, 4, pp. 51–55. Journal of the Virtual Explorer.
Petracchini, L., Antonellini, M., Billi, A., Scrocca, D., 2012. Fault development through fractured pelagic carbonates of the Cingoli anticline, Italy: possible analog for subsurface fluid-conductive fractures. J. Struct. Geol. 45, 21–37.
Petracchini, L., Antonellini, M., Billi, A., Scrocca, D., 2015. Syn-thrusting polygonal normal faults exposed in the hinge of the Cingoli anticline, northern Apennines, Italy. Front. Earth Sci. 3, 67. http://dx.doi.org/10.3389/feart.2015.00067.
Reitman, N.G., Bennett, S.E., Gold, R.D., Briggs, R.W., DuRoss, C.B., 2015. High-resolution trench photomosaics from image-based modeling: workflow and error analysis. Bull. Seismol. Soc. Am. 105, 2354–2366.
Remondino, F., El-Hakim, S., 2006. Image-based 3D modelling: a review. Photogramm. Rec. 21, 269–291.
Schlische, R.W., 1995. Geometry and origin of fault-related folds in extensional settings. AAPG Bull. 79, 1661–1678.
Szeliski, R., 2010. Computer Vision: Algorithms and Applications. Springer-Verlag, London.
Tanner, P.W., 1989. The flexural-slip mechanism. J. Struct. Geol. 11, 635–655.
Tavani, S., Storti, F., Salvini, F., 2006. Double-edge fault-propagation folding: geometry and kinematics. J. Struct. Geol. 28, 19–35.
Tavani, S., Arbues, P., Snidero, M., Carrera, N., Muñoz, J.A., 2011. Open plot project: an open-source toolkit for 3-D structural data analysis. Solid Earth 2, 53–63.
Tavani, S., Storti, F., Bausa, J., Muñoz, J.A., 2012. Late thrusting extensional collapse at the mountain front of the northern Apennines (Italy). Tectonics 31. TC4019.
Tavani, S., Granado, P., Corradetti, A., Girundo, M., Iannace, A., Arbués, P., Muñoz, J.A., Mazzoli, S., 2014. Building a virtual outcrop, extracting geological information from it, and sharing the results in Google Earth via OpenPlot and Photoscan: an example from the Khaviz Anticline (Iran). Comput. Geosci. 63, 44–53.
Tavani, S., López, B., Muñoz, J.A., 2015. extensional fold-related fracturing in the armeña rollover (Cotiella Massif, Southern Pyrenees). Ital. J. Geosci. 134, 458–473.
Torvela, T., Bond, C.E., 2011. Do experts use idealised structural models? insights from a deepwater fold-thrust belt. J. Struct. Geol. 33, 51–58.
Trinks, I., Clegg, P., McCaffrey, K.J.W., Jones, R.R., Hobbs, R., Holdsworth, R.E., Holliman, N., Imber, J., Waggot, S., Wilson, R.W., 2006. Mapping and analysing virtual outcrops. Vis. Geosci. 10, 13–19.
Ullman, S., 1979. The interpretation of structure from motion. Proc. R. Soc. Lond. B (203), 405–426.
Verhoeven, G., 2011. Taking computer vision aloft - archaeological three-dimensional reconstructions from aerial photographs with PhotoScan. Archaeol. Prospect. 18, 67–73.
Williams, G., Chapman, T., 1983. Strains developed in the hanging-walls of thrusts due to their slip/propagation rate: a dislocation model. J. Struct. Geol. 5, 563–571.
Withjack, M.O., Olson, J., Peterson, E., 1990. Experimental models of extensional forced folds. AAPG Bull. 74, 1038–1054.
Xu, X., Aiken, C., Bhattacharya, J.P., Corbeanu, R.M., Nielsen, K.C., McMechan, G.A., Abdelsalam, M.G., 2000. Creating Virtual 3-D Outcrop: Leading Edge, vol. 19, pp. 197–202.
Zehnder, A.T., Allmendinger, R.W., 2000. Velocity field for the trishear model. J. Struct. Geol. 22, 1009–1014.